ecoPETROL

ctyf@ecopetrol.com.co

CHARACTERIZATION OF A GROUND PENETRATING RADAR SHIELDED ANTENNA USING LABORATORY MEASUREMENTS, FDTD MODELING AND SWARM GLOBAL OPTIMIZATION

CARACTERIZACIÓN DE UNA ANTENA BLINDADA DE RADAR DE PENETRACIÓN TERRESTRE UTILIZANDO MEDICIONES DE LABORATORIO, MODELADO FDTD Y OPTIMIZACIÓN GLOBAL DE ENJAMBRE

Andrés-Fernando Plata-Galvis[1], Jheyston-Omar Serrano-Luna[2], Ana-Beatriz Ramirez-Silva[2] and Sergio-Alberto Abreo-Carrillo[2]

ABSTRACT

Full Waveform Inversion (FWI) is an optimization method that retrieves high-quality images of the ground's internal electromagnetic properties, such as permittivity, permeability, or conductivity. FWI requirements include an initial subsurface image of the parameters (starting point models), a wave propagation model, a cost function, and the source wavelet used during data acquisition. Usually, the source wavelet is estimated from the acquired data, or modelled from the antenna characteristics. In this study, the materials of the shielded antenna of a commercial Ground Penetrating Radar (GPR), developed by GSSI, are estimated using a global optimization method, from the observation measurements of the source signal. The estimated source is then used to model the wave propagation of the electromagnetic signal, and to estimate the electromagnetic parameters of the SEAM model via FWI. Experimental results show that the soil characteristics with the estimated source and pattern radiations retrieve better quality images than the inversion when the radiation pattern is neglected. In fact, the impact of using the correct source during the inversion is more evident when the initial model is distant from the correct solution.

RESUMEN

La inversión de forma de onda completa (FWI) es un método de optimización que permite obtener imágenes de alta calidad de las propiedades electromagnéticas internas del suelo, como la permitividad, permeabilidad o conductividad. La FWI requiere una imagen inicial del subsuelo (punto de partida), una ecuación de onda para modelar la propagación de las ondas, una función de costo y la ondícula fuente utilizada en la adquisición de los datos. Por lo general, la ondícula de la fuente se estima a partir de los datos adquiridos o se modela a partir de las características de la antena. En este estudio, se estiman los materiales de una antena blindada de radar de penetración terrestre (GPR) comercial, desarrollado por GSSI, utilizando un método de optimización global. La fuente estimada se utiliza para modelar la propagación de las ondas electromagnéticas y para estimar los parámetros electromagnéticos del modelo SEAM a través de la FWI. Los resultados experimentales muestran que la inversión que incluye la fuente estimada y el patrón de radiación produce imágenes de mejor calidad que la inversión que ignora el patrón de radiación. De hecho, el impacto de usar la fuente correcta durante la inversión es más evidente cuando el modelo inicial está lejos de la solución correcta.

KEYWORDS / PALABRAS CLAVE

GPR | FWI | PSO | Radiation pattern.
GPR | FW | PSO | Patrones de Radiación.

AFFILIATION

*[1]National Institute of Astrophysics, Optics and Electronics, Electronic Coordination. Santa María Tonantzintla, Puebla, México
[2]Industrial University of Santander, Faculty of Physical-Mechanical Engineering. School of Electrical, Electronic and Telecommunications Engineering. Bucaramanga, Santander, Colombia
email: jheyston.serrano@e3t.uis.edu.co.*

1. INTRODUCTION

The Ground Penetrating Radar (GPR) provides an accurate and non-destructive solution for estimating the subsurface electromagnetic parameters through the propagation of electromagnetic waves [1]. GPR systems provide real-time analysis, allowing users to safely identify features and objects before drilling or trenching, in such manner that environmental hazards can be avoided.

With the acquired data, the electromagnetic characteristics of the soil (e.g., permittivity, permeability, and conductivity) can be estimated via Full Waveform Inversion (FWI). FWI is an iterative local optimization method that uses a cost function to minimize a distance between the observed data (measured in the field) and the modelled data (obtained by simulation). FWI requires an initial model of subsurface parameters with enough low-wavenumber information, and the signature of the source used during the data acquisition process. Those requirements enable the accurate reconstruction of the underground parameters in FWI. [2]. Including the radiation properties of the antenna in the wave modelling also provides simulated data that resembles the observed data.

Different methods have been used to estimate the source signature for FWI, such as the characterization of the antenna as an infinitesimal dipole, where the energy in TE mode is distributed uniformly for any angle [3], or the signature estimation from the acquired data using the adjoint state method [4], the variable projection method [5], [6] and gradient-based optimization methods [7]. Other proposed methods are reverse-time propagation [8], and the deconvolution of radar data with the parameters system [9].

In this paper, the source signature is obtained by estimating the internal electromagnetic parameters of the GSSI shielded antenna. The parameter estimation problem is formulated as a global optimization issue that compares the simulated electric field (R_{xmod}) with the measured electric field (R_{xobs}) for a set of possible parameter values. The inverse problem is solved using a global optimization algorithm called Particle Swarm Optimization (PSO). This method generates particles with the possible values for the internal parameters of the antenna at random in a predefined search space [10]. The global optimization algorithm compares R_{xobs} and R_{xmod} using two metrics: one in time domain, and the other in frequency domain. The antenna used in this study is a commercial GSSI brand GPR with an operating frequency of *400* [MHz]. The antenna's pattern that describes the energy radiation out into the ground is obtained from the estimated internal parameters of the antenna. Such radiation pattern is then included in the electromagnetic wave propagation and the inversion process.

The soil parameter model used in this paper to test the inversion process is the SEG Advanced Modelling (SEAM) Foothills model [11]. This model was inspired by the Andes mountains in Colombia with compressive tectonics [11].

This paper is divided in four sections. The theoretical framework for both inverse problems: the antenna parameters and FWI, is presented in the first section. Then, a methodology for the estimation of the internal parameters of the antenna and its use in FWI is presented. The next section shows the experimental results of the commercial GSSI antenna characterization, and the estimation of the soil parameters. Finally, the last section gives a brief discussion and conclusions on the proposed methods.

2. THEORETICAL FRAMEWORK

A GPR system mainly consists of three instruments: the control unit, a display system, and the transmitter (Tx) and receiver (Rx) antennas [12]. The commercial system, designed and built by the GSSI at *400* [MHz], is shielded and the Tx-Rx antennas have a single-channel and short-offset configuration. The shielded system is used in GPR applications where the distance between both Tx and Rx antennas is fixed. The internal geometry of a shielded antenna is depicted in Figure 1. The parameters *W*, *L*, and *h* are *6* [cm]. The distance between both antennas, known as the offset, is *16.2* [cm]. The electromagnetic pulse generated by the antenna, considering the internal geometry and its electromagnetic properties, is modelled using the *gprMax* commercial software [13].

The estimation of the electromagnetic properties of the antenna is based on the workflow shown in Figure 2. An electric field is measured at the receiver antenna, and it is called R_{xobs}. A simulated electric field is obtained using the *gprMax* commercial software, and it is called R_{xmod} [14]. The simulated electric field at the receiver antenna, is a function of the electromagnetic parameters of the antenna: the relative permittivity of the absorbent barrier, ε_r(abs); the relative conductivity of the absorbent barrier, σ_r(abs); the relative permittivity of the Printed Circuit Board (PCB), ε_r(PCB); the relative permittivity of the housing, ε_r(housing); and the Tx and Rx resistance.
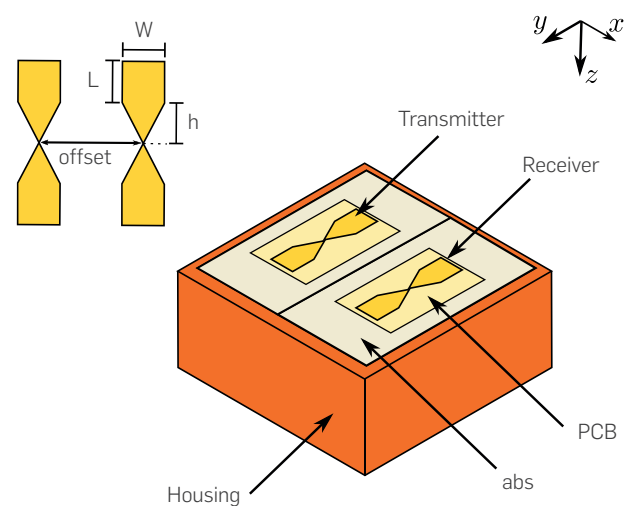

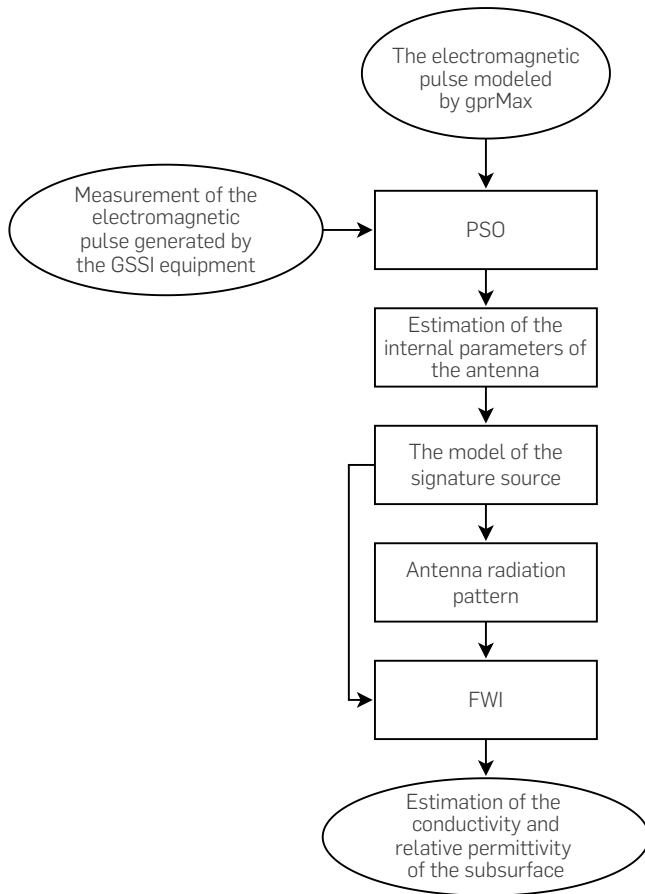**Figure 1.** Internal geometry of the shielded GSSI antenna at *400* [MHz].

Figure 2. Methodology for the estimation of the internal parameters of the shielded antenna.

The *gprMax* software simulates the wave propagation of the source, based on the discretized version of the following time domain wave equations,

$$\frac{\partial E_x}{\partial t} = \frac{1}{\varepsilon}\left(\frac{\partial H_z}{\partial y} - \frac{\partial H_y}{\partial z} - J_{sx} - \sigma E_x\right),$$

$$\frac{\partial H_x}{\partial t} = \frac{1}{\mu}\left(\frac{\partial E_y}{\partial z} - \frac{\partial E_z}{\partial y} - M_{sx} - \sigma^* H_x\right),$$

$$\frac{\partial E_y}{\partial t} = \frac{1}{\varepsilon}\left(\frac{\partial H_x}{\partial z} - \frac{\partial H_z}{\partial x} - J_{sy} - \sigma E_y\right),$$

$$\frac{\partial H_y}{\partial t} = \frac{1}{\mu}\left(\frac{\partial E_z}{\partial x} - \frac{\partial E_x}{\partial z} - M_{sy} - \sigma^* H_y\right),$$

$$\frac{\partial E_z}{\partial t} = \frac{1}{\varepsilon}\left(\frac{\partial H_z}{\partial x} - \frac{\partial H_x}{\partial y} - J_{sz} - \sigma E_z\right),$$

$$\frac{\partial H_z}{\partial t} = \frac{1}{\mu}\left(\frac{\partial E_x}{\partial y} - \frac{\partial E_y}{\partial x} - M_{sz} - \sigma^* H_z\right),$$

(1)

where ε, σ, μ are the permittivity [F/m], permeability [H/m] and conductivity [S/m], respectively; σ^* is the equivalent magnetic loss [Ω/m]; E_x, E_y, E_z are the electric fields in the direction x, y and z,

respectively; H_x, H_y, H_z are the magnetic fields in the direction x, y and z respectively; J_{sx}, J_{sy} and J_{sz} are the densities of electric current at x, y and z, respectively; and M_{sx}, M_{sy}, M_{sz} are the magnetic current densities at x, y and z, respectively [15]. In all experiments $\mu=1$ since the materials are not magnetic, and $\sigma^*=0$ because the magnetic losses are zero. On the other hand, the excitation and reception of the electric current density is only applied in the y-direction due to the orientation of the antennas; therefore $J_{sx}=0$ and $J_{sz}=0$.
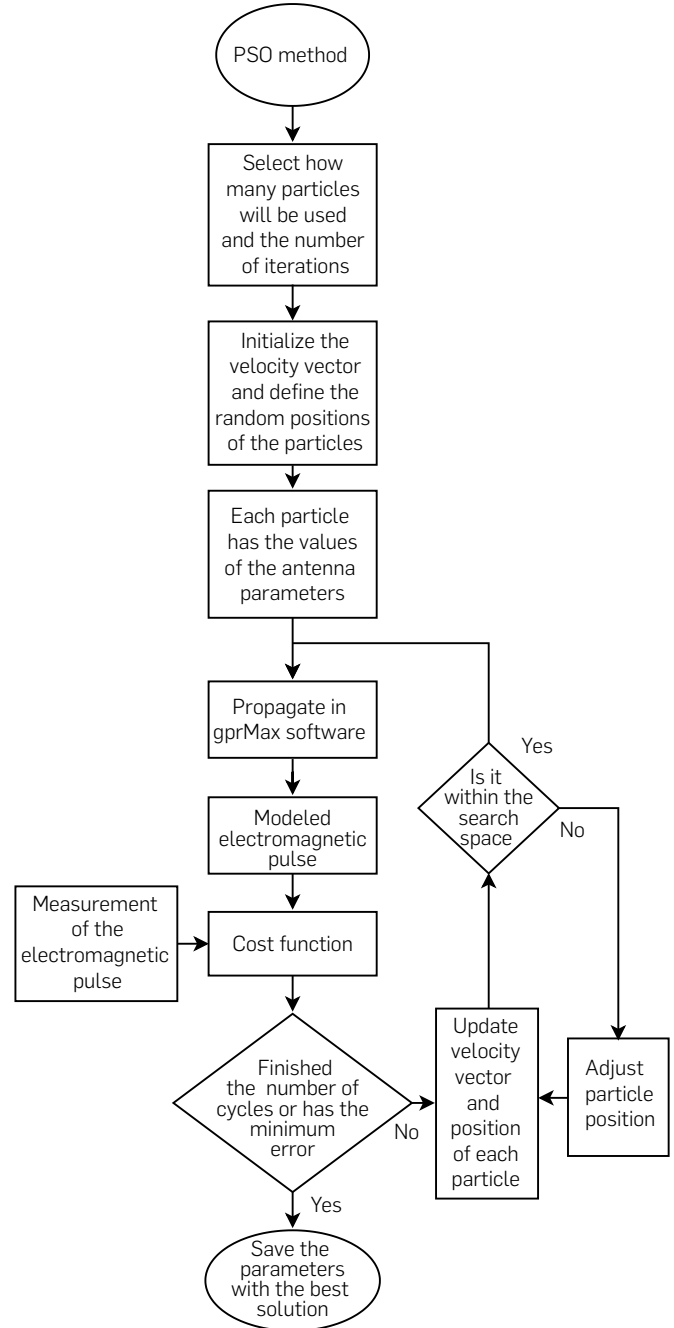

Figure 2. PSO inversion process to estimate the internal antenna parameters.

The Particle Swarm Global Optimization (PSO) method seeks the best combination of the internal parameters to minimize a given cost function (see Figure 3). In this paper, two metrics are proposed to measure the similarity between the measured electric field R_{xobs} and the simulated electric field R_{xmod}. First, the cross-correlation in time domain is used [16]. The cross-correlation equation is given by,

$$r = \frac{\sum_{i=1}^{n}(R_{xobs}(i)-\overline{R_{xobs}})(R_{xmod}(i)-\overline{R_{xmod}})}{\sqrt{(\sum_{i=1}^{n}(R_{xobs}(i)-\overline{R_{xobs}})^2)(\sum_{i=1}^{n}(R_{xmod}(i)-\overline{R_{xmod}})^2)}}, \quad (2)$$

where $(\overline{R_{xobs}})$ and $(\overline{R_{xmod}})$ are the mean value of R_{xobs} and R_{xmod}, respectively.

A second metric that measures the difference of the maximum values of the amplitude spectrum of R_{xobs} and R_{xmod}, is used in the global optimization method. This is given by,

$$rf = |Max(abs(FFT(R_{xmod}))) \\ - Max(abs(FFT(R_{xobs})))|, \quad (3)$$

where $|\cdot|$ is the modulus, $Max(\cdot)$ is the maximum value, $abs(\cdot)$ is the amplitude spectrum and $FFT(\cdot)$ is the Fast Fourier Transform.

PSO is an iterative method that randomly creates a group of particles, where each particle contains the information of each antenna parameter (see Figure 1). All the particles keep the memory of their best position vector and their velocity vector [17]. In each iteration, a particle velocity adjustment is made, according to the best previous position occupied by the particle (i) and the best position of the group of particles, as it is given by,

$$v(i) = w.v(i) + c_1.r_1\left(M_{local}(i) - X_{position}(i)\right) \\ + c_2.r_2\left(M_{global}(i) - X_{position}(i)\right), \quad (4)$$

where $w=0.3$, $c_1=0.5$ and $c_2=2.05$ are constants of each optimization problem; r_1 and r_2 are random values between 0 and 1; $X_{position}$ is the current position of the particle; M_{global} is the best position of the particle group; and M_{local} is the best position previously occupied by the particle. The position vector is updated with the current position and the new velocity vector as,

$$X_{position} = X_{position}(i) + v(i) \cdot dt. \quad (5)$$

This process is iterative, and it stops when it reaches several iterations or until a minimum error value is obtained. Once the antenna parameters are estimated, its radiation pattern can be obtained. The radiation patterns give the distribution of the energy in the subsurface [3].

One of the challenges addressed in this paper is the estimation of the radiation patterns for a shielded antenna with a fixed offset. The radiation pattern is measured in a spherical coordinate system as shown in FIGURE 4. The radiation pattern is transformed from spherical coordinates to cartesian coordinates such that the electric and magnetic fields can be obtained for each time. For the transform of the coordinates, x, y, and z are defined as: $x=rcos(\varphi)sin(\theta)$, $y=rsin(\varphi)sin(\theta)$, and $z=rcos(\theta)$. The transformed points from spherical to cartesian coordinates are not exact values on the mesh thus requiring an interpolation. In this case, a bilinear interpolation is performed for a given value $f(x,z)$, with x and z being the locations in distance-direction and depth-direction, respectively [18].
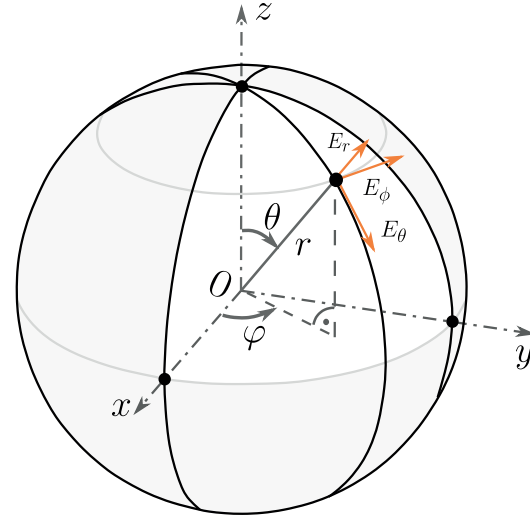

Figure 4. Spherical coordinate system used to transform the radiation pattern to rectangular coordinates.

The pattern radiation generated by the source of the GSSI antenna can be estimated in spherical coordinates by,

$$r = r_1\hat{\imath} + r_2\hat{\jmath} + r_3\hat{k},$$
$$r_1 = \frac{x}{\sqrt{x^2+y^2+z^2}}, \quad \theta_1 = \frac{xz}{\sqrt{x^2+y^2+z^2}\sqrt{x^2+y^2}}, \quad \phi_1 = \frac{-y}{\sqrt{x^2+y^2}},$$
$$r_2 = \frac{y}{\sqrt{x^2+y^2+z^2}}, \quad \theta_2 = \frac{yz}{\sqrt{x^2+y^2+z^2}\sqrt{x^2+y^2}}, \quad \phi_2 = \frac{x}{\sqrt{x^2+y^2}}, \quad (6)$$
$$r_3 = \frac{z}{\sqrt{x^2+y^2+z^2}}, \quad \theta_3 = \frac{-\sqrt{x^2+y^2}}{\sqrt{x^2+y^2+z^2}}, \quad \phi_3 = 0.$$

The electric field in terms of r, θ and ϕ are defined as,

$$E_r = E_x r_1 + E_y r_2 + E_z r_3,$$
$$H_r = H_x r_1 + H_y r_2 + H_z r_3,$$
$$E_\theta = E_x \theta_1 + E_y \theta_2 + E_z \theta_3,$$
$$H_\theta = H_x \theta_1 + H_y \theta_2 + H_z \theta_3, \quad (7)$$
$$E_\phi = E_x \phi_1 + E_y \phi_2 + E_z \phi_3,$$
$$H_\phi = H_x \phi_1 + H_y \phi_2 + H_z \phi_3.$$

The sum of all the squared values of E_θ and H_θ are computed to obtain the radiation plane E and H, respectively. The energy for each plane is given by,

$$\Psi_E = \sum_{t=0}^{T} E_\theta^2, \quad \Psi_H = \sum_{t=0}^{T} H_\theta^2. \quad (8)$$

FULL WAVEFORM INVERSION

The inverse problem estimates the soil parameters $m(\varepsilon_r, \mu_r, \sigma_r)$ from the observations on surface R_{xobs}, the electric field E_y and a known source (J_s). Full Waveform Inversion (FWI) minimizes the l^2- norm squared of the difference between the modeled data $R_{xmod}(m^k)$ and R_{xobs} observed data [19], as follows

$$\Phi(s) = \arg \min_{m^k} \sum_i^{Ns} \frac{1}{2} \left\| R_{xmod}^i(m^k, s) - R_{xobs}^i \right\|_2^2, \quad (9)$$

with

$$R_{xmod}^i(m^k) = RE_y^i, \quad (10)$$

where m^k are the unknown parameters in the k-th iteration, Ns the number of sources, R is the operator that extracts the electromagnetic wavefield E_y at the receiver positions and s is the electromagnetic vector fields $[E_y, H_x, H_z]$. The inverse problem can be solved iteratively by selecting an initial parameters model m^0, and updating it by using Newton-like methods [20], as

$$m^{k+1} = m^k + \alpha_k \Delta m^k, \quad (11)$$

where α_k is the step size and Δm^k at the kth iteration is given by

$$\Delta m^k = -[\mathfrak{h}(m^k)]^{-1} g(m^k). \quad (12)$$

The inverse of the Hessian matrix $[h(m^k)]^{-1}$ and the gradient $g(m^k)$, in the Equation (12) are both evaluated at m^k [21]. As the inverse problem is ill-posed, the cost function given in Equation (9) has several minimums and an inadequate starting point (m^0) will produce convergence to a local minimum.

The electromagnetic wave equations in a non-dispersive and isotropic medium are considered where the fields E_y, H_x and H_z are different from zero. The forward operator is described by

$$\varepsilon_r \varepsilon_0 \frac{\partial E_y}{\partial t} - \frac{\partial H_x}{\partial z} + \frac{\partial H_z}{\partial x} + \sigma_r \sigma_0 E_y - J_s = 0,$$

$$\mu_0 \frac{\partial H_x}{\partial t} - \frac{\partial E_y}{\partial z} = 0, \quad (13)$$

$$\mu_0 \frac{\partial H_z}{\partial t} + \frac{\partial E_y}{\partial x} = 0,$$

where σ_r is the relative conductivity; this relative parameter is a scale setting for the conductivity value, where σ_0 is an arbitrary scale value. The expression for σ_r is as follows $\sigma_r = \sigma/\sigma_0$; ε_r is the relative permittivity; ε_0 and μ_0 are the permittivity and permeability in the vacuum, respectively. For all the experiments, $\varepsilon_0 \cong 8.85 \times 10^{-12}$, $\mu_0 \cong 4\pi \times 10^{-7}$ and $\sigma_0 = 5.56 \times 10^{-4}$.

On the other hand, the adjoint operator for the cost function is defined as

$$\varepsilon_r \varepsilon_0 \frac{\partial \lambda_{E_y}}{\partial t} - \frac{\partial \lambda_{H_x}}{\partial z} + \frac{\partial \lambda_{H_z}}{\partial x} - \sigma_r \sigma_0 \lambda_{E_y} + \frac{\partial \Phi}{\partial s} = 0, \quad (14)$$

$$\mu_0 \frac{\partial \lambda_{H_x}}{\partial t} - \frac{\partial \lambda_{E_y}}{\partial z} = 0, \quad (15)$$

$$\mu_0 \frac{\partial \lambda_{H_z}}{\partial t} + \frac{\partial \lambda_{E_y}}{\partial x} = 0, \quad (16)$$

where $\partial \Phi / \partial s = R_{xmod}(s) - R_{xobs}$. Also, λ_{E_y}, λ_{H_x}, and λ_{H_z} are the adjoint fields for E_y, H_x and H_z, respectively. The following expressions are defined to obtain the gradients for permittivity and conductivity.

$$g(\varepsilon_r) = \int_0^{Tend} \varepsilon_0 \lambda_{E_y} \frac{\partial E_y}{\partial t} dt, \quad (17)$$

$$g(\sigma_r) = \int_0^{Tend} \sigma_0 \lambda_{E_y} E_y dt. \quad (18)$$

3. RESULTS AND ANALYSIS

ESTIMATION OF THE ANTENNA INTERNAL PARAMETERS

The results of the antenna parameters estimation are presented in this section. For the PSO method, a total of 65 experiments were performed. The searching regions for the source and receiver resistance (r) ranges between [1-1000] [Ω]; for ε_r(abs), ε_r(housing) and ε_r(PCB) range between [1-30] [F/m]; and finally, for σ_r(abs) ranges between [0-20] [S/m]. The sample space for all parameters within the searching region is 1×10^{-5}.

The materials of the internal structure of the antenna estimated with the proposed method were r= 49.22 [Ω], ε_r(abs)=3.89, σ_r(abs)=0.02 [S/m], ε_r(PCB) =7.44 [F/m], and ε_r(hdp) = 1.00 [F/m]. The error between R_{xobs} and R_{xmod} using the estimated parameters is 2.65%. Figure 5-a) and 5-b) show the resulting signals in time and frequency, respectively.
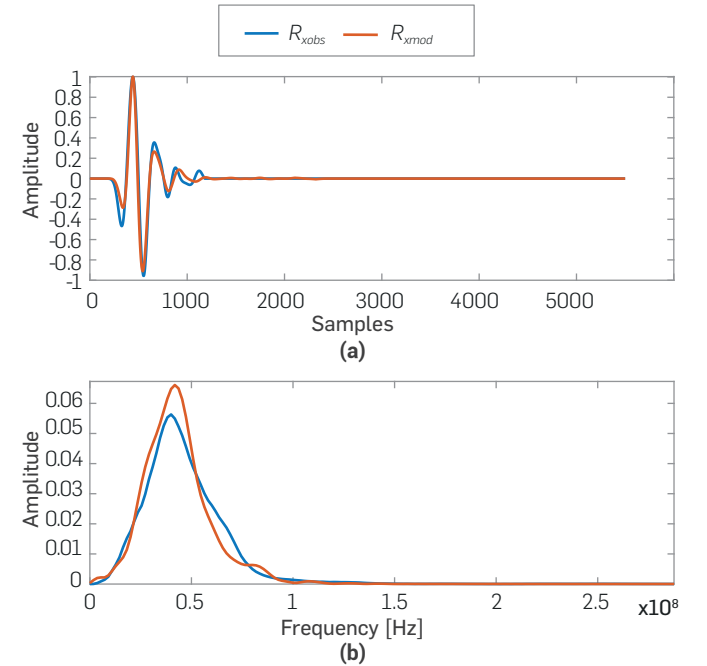

Figure 5. a) R_{xmod} and R_{xobs} in the time domain.
b) Frequency spectrum for R_{xmod} and R_{xobs}.

The bowtie antenna can be represented using a dipole as an approximation. For the case of an y-axis oriented dipole, the radiation pattern will be a toroid as shown in Figure 6-a) and their respective views in the x-z and y-z planes are presented in Figure 6-b) and c), respectively.
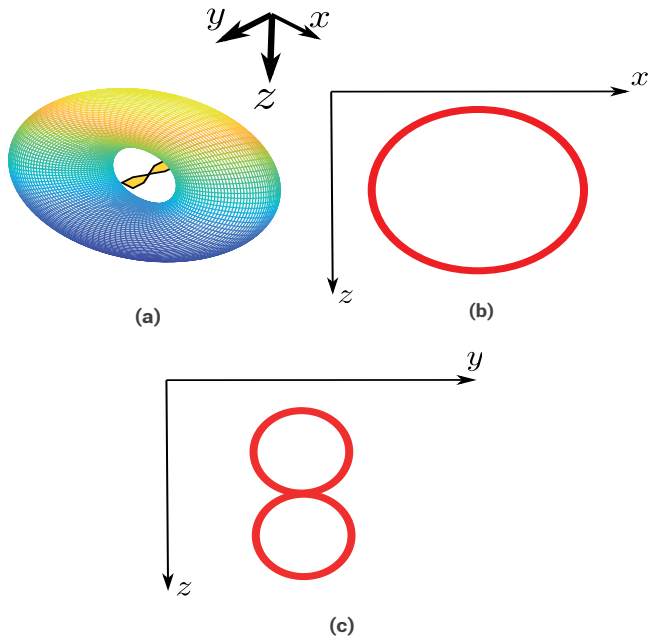
(a)

(b)

(c)

Figure 6. Radiation patterns for an oriented dipole: a) 3D view, b) plane x-z and c) y-z.

The electric and magnetic fields are measured at a radius from 0.2 [m] to 0.9 [m] and a $dr = 0.12$ [m]. The angle of observation ranges from 0 [rad] to 2π [rad] with $d\theta = 0.104$ [rad]. The results, in Figure 7, show the radiation patterns in two-dimensions. However, given the antenna's internal geometry, the energy is attenuated between -60° and 60°. The resulting radiation patterns are included in the propagation of the electromagnetic field, and in the inverse problem. The radiation pattern in cartesian coordinates is shown in Figure 8-a) and 8-c) for two different angles of the slope, but only the radius lower than 0.2 [m] is used in the wave propagation (see Figure 8-b) and 8-d)). The angle of the slope is required due to the rough topography of the SEAM model.

FULL WAVEFORM INVERSION

This section presents the results of estimating the electromagnetic parameters of the source using the estimated source (J_s) and its radiation pattern (P_r). The radiation pattern is included in the wave propagation modelling by multiplying the pattern with the fields E_y, H_x, and H_z, where the electromagnetic equations are those for a non-dispersive and isotropic medium with $\tilde{E}_y = Pr \cdot E_y$, $\tilde{H}_x = Pr \cdot \tilde{H}_x$ and $\tilde{H}_z = Pr \cdot H_z$.

Experiment description: We use the previously estimated radiation pattern of the antenna to simulate the acquisition of GRP data from a single-offset antenna on the surface. The simulated observations
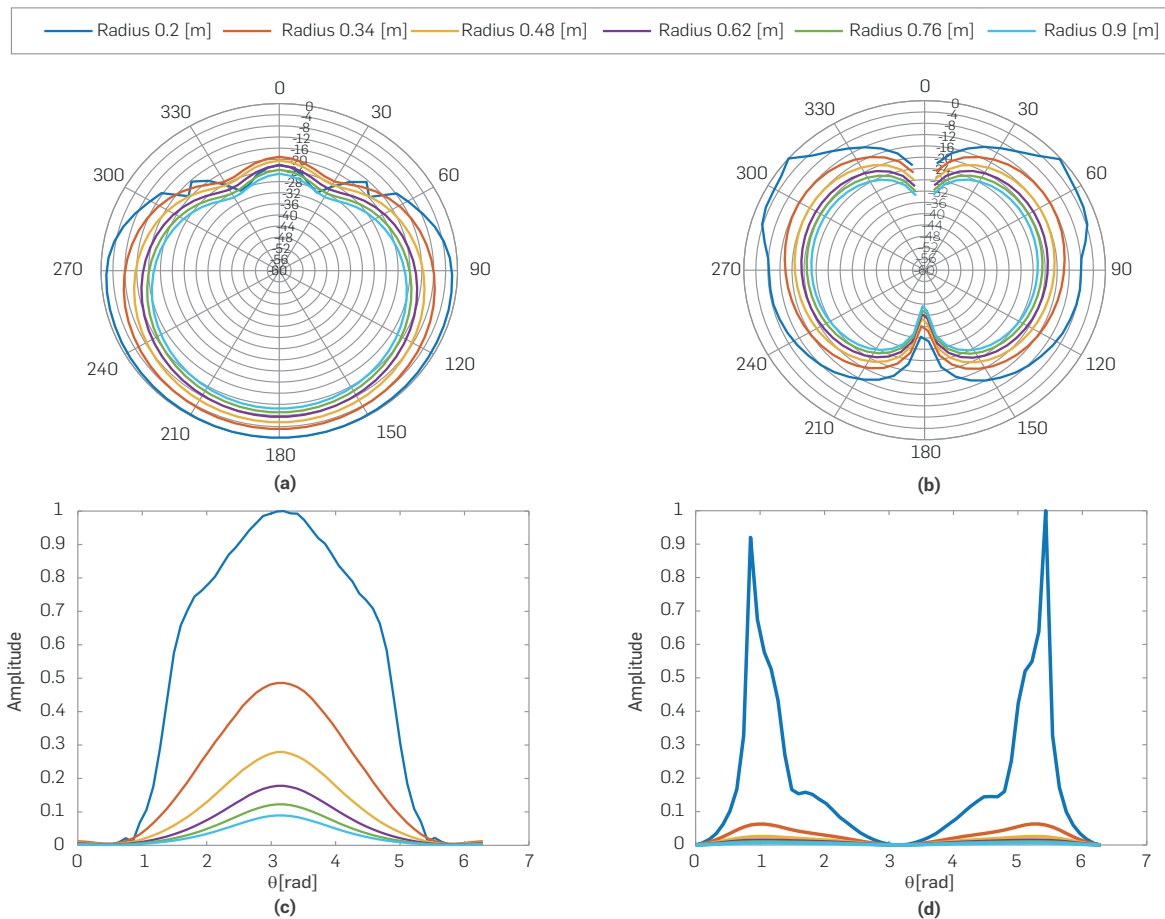

Figure 7. E and H planes of radiation for the shielded antenna at 400 [MHz]. a) and b) show the radiation patterns in polar coordinates (r [dB] vs θ [grades]) for planes E and H, respectively. The radius ranges from 0.2 [m] to 0.9 [m] with a step size of 0.116 [m]. c) and d) show the normalized radiation patterns with respect to the maximum value in planes E and H, respectively
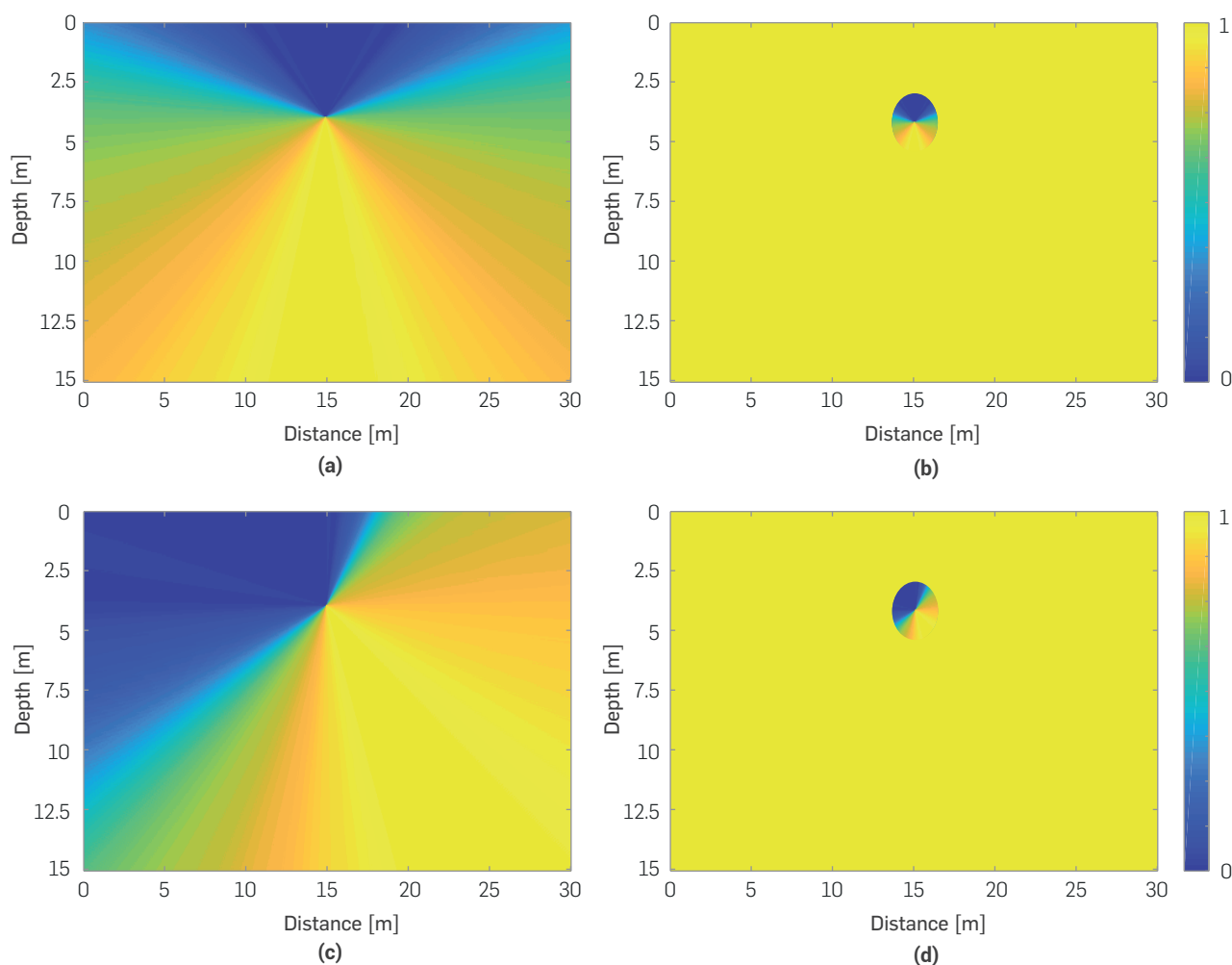
Figure 8. Radiation patterns: a) with an angle of 0° of inclination, b) radiation pattern for a radius less than *0.2* [m] and 0° of inclination, c) with an angle of 39.78° of inclination, d) radiation pattern for radius less than *0.2* [m] and 39.78° of inclination.

are obtained supposing that the source has three different central frequencies: *30* [Mhz], *50* [MHz] and *100* [MHz]. For the wave propagation of the source with a central frequency of *100* [MHz] using the SEAM model, the spatial step in both dimensions is set to *0.05* [m], the time step is *0.06* [ns], and the total number of time samples is *3000* [10]. The model has *30* [m] in distance and *15.05* [m] in depth. The number of sources is *260* and they are equally distributed at *25* [cm] at the surface. The receiving antenna is located at *15* [cm] from the surface.

Figure 9-a), 9-b) and 9-c) show the wave propagation at the 500th time sample, and Figure 9-c), 9-d) and 9-f) present the wave propagation at the 1000th time sample. Figure 9-a) and 9-d) show the propagation including the radiation pattern at 0° of inclination. Figure 9-b) and 9-e) depict the propagation without considering the radiation pattern, and Figure 9-c) and 9-f) depict the propagation including an angle of inclination of 39.78° due to the slope of the rough topography. Notice at the red ovals in the Figure 9-a), 9-b) and 9-c) that the airwave energy distribution changes when the radiation pattern is included.

The reconstruction of the electromagnetic properties of the SEAM model is studied for three different scenarios: 1) The SEAM model has a rough topography, and the initial model is a smooth version of the original model. 2) The SEAM model has a rough topography, and the initial model is a constant value. 3) The SEAM model has a flat topography, and the initial model is a smooth version of the original model. The proposed tests seek to study the effects of topography in the model and the initial models for permittivity and conductivity.

Figures 10, 11, and 12 show the estimated models for the three proposed scenarios. In all tests, 30 iterations are performed for each central frequency of the source. The first row in Figures 10, 11 and 12, is the relative permittivity parameter, and the second row is the relative conductivity parameter. Further, the first column presents the original models; the second column shows the initial models; the third column gives the FWI results obtained using the radiation pattern, and the last column shows the results of FWI, not including the radiation pattern.
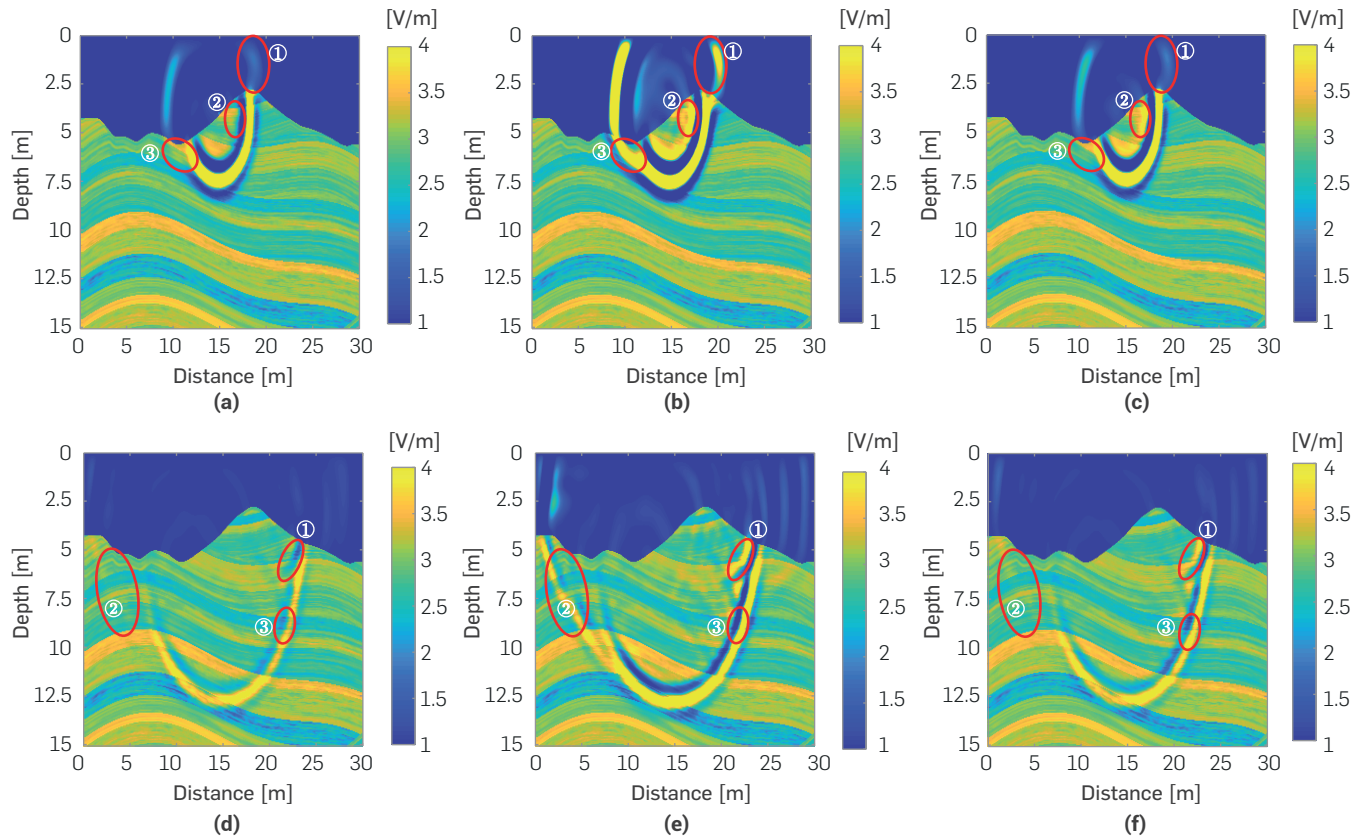
Figure 9. Propagation of the electromagnetic wavefront. First row: 500th time sample. Second row: 1000th time sample. a) Including the radiation pattern at 0° of inclination, b) without radiation pattern, c) including the radiation pattern at 39.78° of inclination.
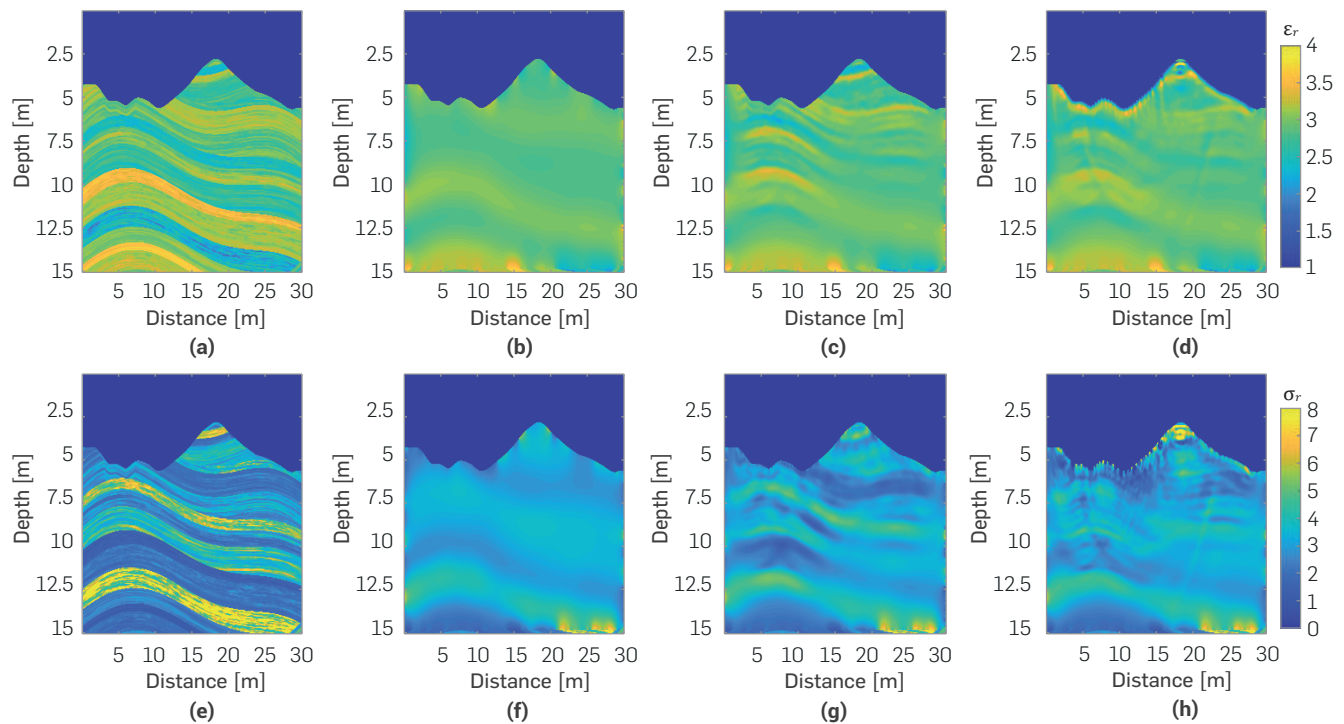

Figure 10. FWI results considering the radiation pattern. The first row is the relative conductivity, and the second row is the relative permittivity. a) and e) original models, b) and f) initial models, c) and g) models obtained after FWI multi-scale using the radiation pattern and d) and h) models obtained after FWI multi-scale without the radiation pattern.

The Peak Signal to Noise Ratio (PSNR) is used as quantitative error measurement between the ground real image and the estimated images. The PSNR for the initial models are *24.29* [dB] for permittivity and *24.56* [dB] for conductivity. When the radiation pattern is included, the resulting images reach PSNR values of *25.66* [dB] for relative permittivity (see Figure 10-c)) and *25.59* [dB] for conductivity (see Figure 10-g)). On the other hand, the images obtained when the radiation pattern is not included reach a PSNR of *23.69* [dB] for permittivity (see Figure 10-d)), and *22.87* [dB] for conductivity (see Figure 10-h)).

Figure 11 shows the estimated models when uniform initial models are used. The initial model has constant values of relative permittivity of ε_r=3 and relative conductivity of σ_r=2.28. Visually, the images when the radiation pattern is included (see Figure 11-c) and g)) are slightly better than when the radiation pattern is not included (see Figure 11-d) and h)). Note in Figure 11-c) and 11-g) that the first layers of the SEAM model can be observed whereas, if the radiation pattern is not adequately included, then the solution produces artifacts in the shallow area in both parameters, which lead to erroneous visual interpretations. Nonetheless, the quantitative PSNR values are very similar in both cases; when the radiation patterns are included, the estimated model has PSNR values of *13.85* [dB] for the relative permittivity and *21.24* [dB] for the relative conductivity, and when the radiation pattern is not included, the PSNR values are *13.77* [dB] and *21.37* [dB] for relative permittivity and relative conductivity, respectively.

Figure 12 shows the estimated electromagnetic models when the topography of the SEAM model is flat. Note that for this experiment, the rough topography is not considered, but the antenna radiation pattern has an angle of inclination of *0* degrees. Figure 12-c) and 12-g) show a good quality image when the radiation pattern is included and the PSNR values are *26.52* [dB] for the relative permittivity and *26.19* [dB] for the relative conductivity. When the radiation pattern is not included, there are artifact effects on the near surface layer, which result in low quality imaging. The PSNR values for these images are *23.91* [dB] for the relative permittivity, and *23.69* [dB] for the relative conductivity.

Finally, Figure 13 depicts the error function for the three different scenarios studied in this paper. Note in this figure that the error is always less when the radiation pattern is included in the source wave propagation. Also, since the central frequency of the source changes every *30* iterations, the error increases at iterations *31* and *61*, and then decreases again. This behaviour is equal in all experiments. The figure on the left depicts the cost function when the SEAM model has a rough topography, and the initial model is a smooth version of the original model. The figure in the middle is the cost function when the SEAM model has a rough topography, and the initial model is a constant value. Lastly, the image on the right is the cost function when the SEAM model has a flat topography, and the initial model is a smooth version of the original model.
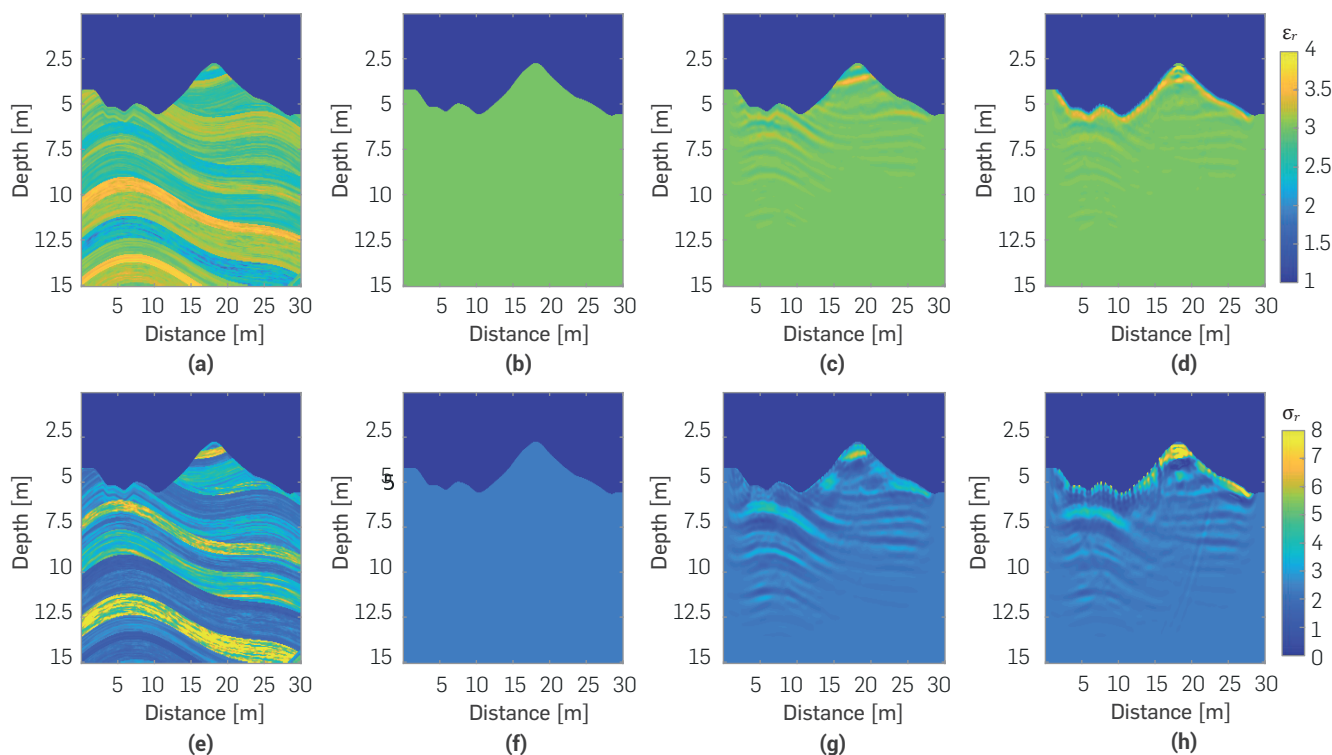

Figure 11. Estimated electromagnetic models using FWI. First row: relative permittivity. Second row: relative conductivity. a) and e) original models, b) and f) uniform initial models, c) and g) models obtained when the radiation pattern is included; and d) and h) models obtained when the radiation pattern is not included.
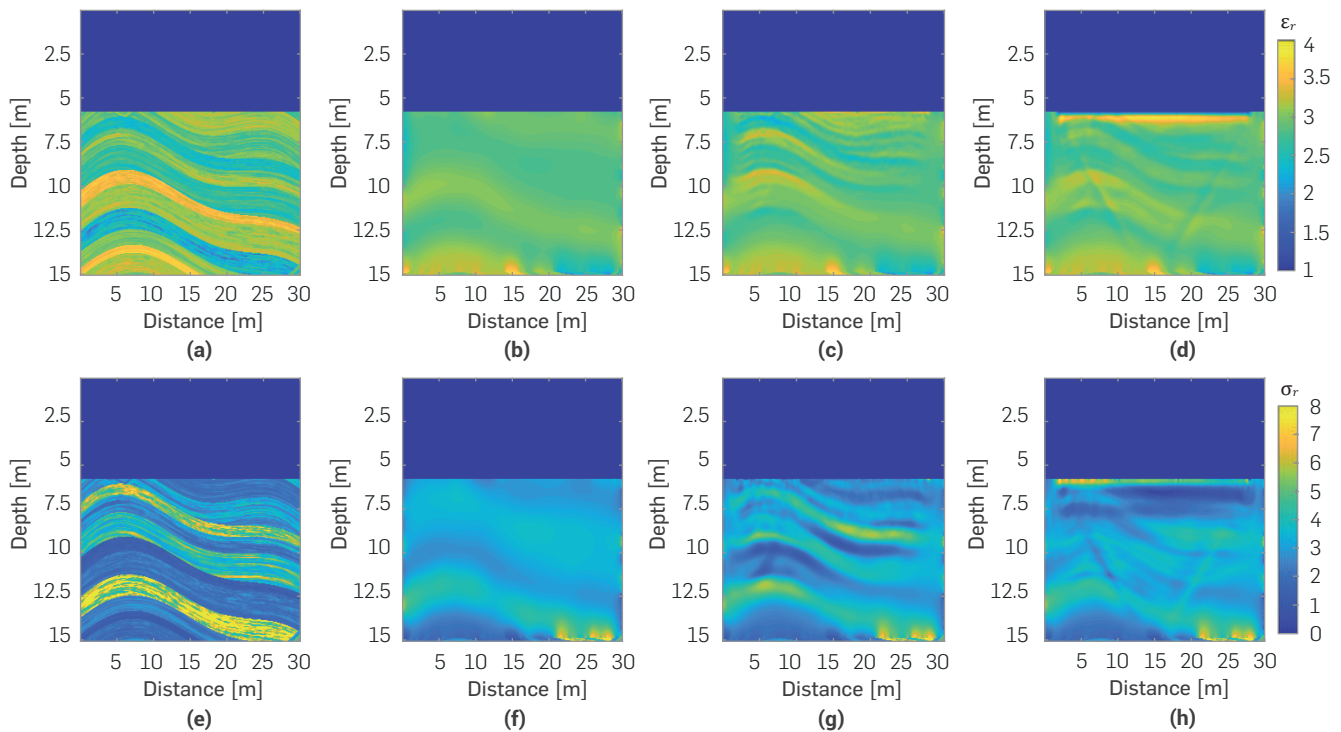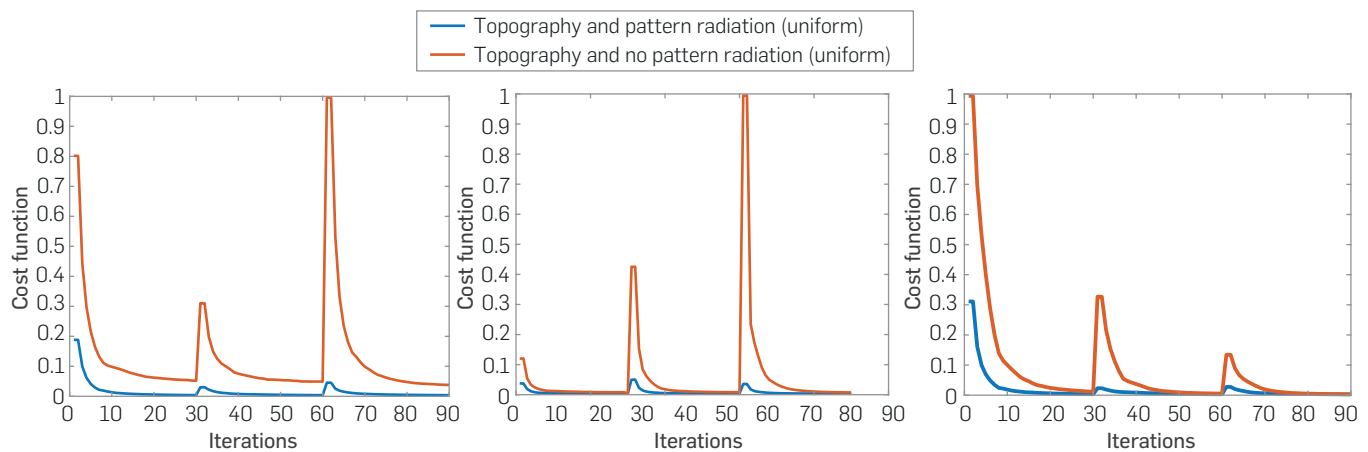
Figure 12. Estimated electromagnetic models using FWI. First row: relative permittivity. Second row: relative conductivity. a) and e) original models, b) and f) initial models, c) and g) models obtained when the radiation pattern is included; and d) and h) models obtained when the radiation pattern is not included.

Figure 13. Error functions for three different scenarios. Left: the SEAM model has a rough topography, and the initial model is a smooth version of the original model. Middle: the SEAM model has a rough topography, and the initial model is a constant value. Right: the SEAM model has a flat topography, and the initial model is a smooth version of the original model.

CONCLUSIONS AND DISCUSSION

In this work, a global optimization method is proposed to find the internal physical parameters of a shielded antenna. The search for the best solution is based on two metrics: the maximum correlation between the observed and modelled signals, and the minimum difference of the spectrum amplitudes of the observed and modelled signals. The estimated parameters of the antenna are used to generate the antenna radiation pattern, which is used to simulate the wave propagation of a source throughout the SEAM synthetic model. Three different scenarios for the reconstruction of the ground electromagnetic parameters were evaluated: first, when the SEAM model has a rough topography, and the initial model is a smooth version of the original model; second, when the SEAM model has

a rough topography, and the initial model is a constant value; and third, when the SEAM model has a flat topography, and the initial model is a smooth version of the original model

.
In sum, characterizing the source signal and including the correct radiation pattern in the synthetic inversion experiments was found to help inversion to converge to better quality images, either with flat or rough topography. The difference between the reconstructed images with radiation pattern and without radiation pattern is

approximated *3* [dB] when the initial model is a smooth version of the correct solution.

When the initial model is constant, there is no significant difference in imaging when adding the radiation pattern. Hence, including the radiation pattern does not improve the solution if there is a poor starting model, as they do not provide enough low wavenumber information of the solution and, thus, reaching the correct solution would not be possible for FWI.

REFERENCES

[1] Daniels, D. J. (2004). *Ground penetrating radar.* 2nd ed. London, United Kingdom: The institution of Electrical Engineers. doi: https://doi.org/10.1049/PBRA015E

[2] Lavoué, F., R. Brossier, L. Métivier, S. Garambois, and J. Virieux. (2014). Two-dimensional permittivity and conductivity imaging by full waveform inversion of multioffset GPR data: A frequency-domain quasi-Newton approach, *Geophys. J. Int.*, 197(1), 248–268. doi: https://doi.org/10.1093/gji/ggt528

[3] Diamanti, N. and A. P. Annan. (2013). Characterizing the energy distribution around GPR antennas, J. *Appl. Geophys.*, 99, 83–90. doi: https://doi.org/10.1016/j.jappgeo.2013.08.001

[4] Plessix, R. E. (2006). A review of the adjoint-state method for computing the gradient of a functional with geophysical applications, *Geophys. J. Int.*, 167(2), 495–503. doi: https://doi.org/10.1111/j.1365-246X.2006.02978.x

[5] Golub, G. and V. Pereyra. (2003). Separable nonlinear least squares: The variable projection method and its applications, *Inverse Probl.*, 19(2). doi: https://doi.org/10.1088/0266-5611/19/2/201

[6] Fang, Z., R. Wang, and F. J. Herrmann. (2018). Source estimation for wavefield-reconstruction inversion, *Geophysics*, 83(4), R345–R359. doi: https://doi.org/10.1190/geo2017-0700.1

[7] Liu, J., A. Abubakar, T. M. Habashy, D. Alumbaugh, E. Nichols, and G. Gao. (2018). Nonlinear inversion approaches for cross-well electromagnetic data collected in cased-wells, 78th Soc. *Explor. Geophys. Int. Expo. Annu. Meet.* SEG 2008, 1, 304–308. doi: https://doi.org/10.1190/1.3054810

[8] Zhang, P., R. Gao, L. Han, and Z. Lu. (2021). Refraction waves full waveform inversion of deep reflection seismic profiles in the central part of Lhasa Terrane, *Tectonophysics*, 803(September 2020), 228761. doi: https://doi.org/10.1016/j.tecto.2021.228761

[9] Ernst, J. R., A. G. Green, H. Maurer, and K. Holliger. (2007). Application of a new 2D time-domain full-waveform inversion scheme to crosshole radar data, *Geophysics*, 72(5). doi: https://doi.org/10.1190/1.2761848

[10] Russell, E. and S. Yuhui. (2001). Particle swarm optimization: Developments, applications and resources., *Inst. Electr. Electron. Eng.*, 1, 81–86. doi: http://dx.doi.org/10.1109/CEC.2001.934374

[11] Regone, C., J. Stefani, P. Wang, C. Gerea, G. Gonzalez, and M. Oristaglio. (2017). Geologic model building in SEAM Phase II-Land seismic challenges, *Lead. Edge*, 36(9), 738–749. doi: https://doi.org/10.1190/tle36090738.1

[12] Jol, H. M. (2009). *Ground penetrating radar: theory and applications*, 1st ed. Amsterdam, The Netherlands: Elsevier B.V. doi: https://doi.org/10.1016/B978-0-444-53348-7.00017-X

[13] Stadler, S. and J. Igel. (2018). A numerical study on using guided GPR waves along metallic cylinders in boreholes for permittivity sounding, 2018 *17th Int. Conf. Gr. Penetrating Radar*, GPR 2018. doi: https://doi.org/10.1109/ICGPR.2018.8441666

[14] Warren, C., A. Giannopoulos, and I. Giannakis. (2016). gprmax: Open source software to simulate electromagnetic wave propagation for ground penetrating radar, *Comput. Phys. Commun.*, 209, 163–170. doi: https://doi.org/10.1016/j.cpc.2016.08.020

[15] Taflove, A. and S. C. Hagness. (2005). *Computational electrodynamics: the finite-difference time-domain method*, 3rd ed. London, United Kingdom: Artech house, INC. doi: https://doi.org/10.1002/0471654507.eme123

[16] Canavos, G., P. Meyer, S. Murray, and M. Scheaffer. (1988). *Probability and statistics: applications and methods*, 1st ed.28. Naucalpan de Juárez, México: McGraw-Hill. ISBN: 968-451-856-0

[17] Sen, M. and P. Stoffa. (2013). *Global optimization methods in geophysical inversion*, 2nd ed. New York, United States: cambridge university press. doi: https://doi.org/10.1017/CBO9780511997570

[18] Press, W., S. Teukolsky, and W. Vetterling. (1997). *Numerical recipes in C: the art of scientific computing*, 2nd ed. New York, United States: cambridge university press.
[19] Virieux, J. and S. Operto. (2009). An overview of full-waveform inversion in exploration geophysics, *Geophysics*, 74, 1–26. doi: https://doi.org/10.1190/1.3238367

[20] Goldstein, A. (1965). On newton's method, *Numer. Math.*, 7, 391–393. doi: https://doi.org/10.1007/BF01436251

[21] Yong, M. (2012). Waveform-based velocity estimation from reflection seismic data, Ph.D. thesis, Dept. Geophysics, Colorado School of Mines, United States.

AUTHORS

Andrés-Fernando Plata-Galvis
Affiliation: Instituto Nacional de Astrofísica, Óptica y Electrónica, Puebla, 72840, México
ORCID: https://orcid.org/0000-0002-3981-3119
e-mail: aplata@inaoe.mx

Jheyston-Omar Serrano-Luna
Affiliation: Universidad Industrial de Santander, Santander, 680002, Colombia
ORCID: https://orcid.org/0000-0002-4834-0325
e-mail: jheyston.serrano@e3t.uis.edu.co

Ana-Beatriz Ramirez-Silva
Affiliation: Universidad Industrial de Santander, Santander, 680002, Colombia
ORCID: https://orcid.org/0000-0002-0025-6423
e-mail: anaberam@uis.edu.co

Sergio-Alberto Abreo-Carrillo
Affiliation: Universidad Industrial de Santander, Santander, 680002, Colombia
ORCID: https://orcid.org/0000-0001-7094-4734
e-mail: sergio.abreo@e3t.uis.edu.co

EN ECOPETROL ESTAMOS COMPROMETIDOS CON LA TRANSICIÓN ENERGÉTICA

POR ESO SEGUIMOS

SUMANDO ACCIONES PARA LOGRARLO

+8 PARQUES SOLARES

INVESTIGACIONES DE ENERGÍA EÓLICA

CO₂

COMPROMISO CERO EMISIONES NETAS DE CARBONO EN 2050

H2

INICIAMOS PILOTO DE HIDRÓGENO VERDE

USEMOS NUESTRA ENERGÍA PARA CONSTRUIR UN PAÍS DE TODOS, PARA TODOS.

ecopetrol